DEM–LBM numerical modeling of submerged cohesive granular discharges

Jianhua Fan, Li-Hua Luu, Gildas Noury, Pierre Philippe

Noname manuscript No.
(will be inserted by the editor)

DEM-LBM numerical modeling of submerged cohesive granular discharges

Jianhua Fan · Li-Hua Luu · Gildas Noury · Pierre Philippe

Received: date / Accepted: date

Abstract Empirical predictions of discharge rates for dry non-cohesive grains are commonly based on the Beverloo law (1961). The present work extends this practical configuration to submerged and cohesive cases to investigate the flow behavior of granular media with applications in the geophysical process of sinkhole formation. The analysis of the hydrostatic collapse of soil in the presence of underground conduits is performed with a 2D GPU-parallelized simulation coupling the lattice Boltzmann method (LBM) and the discrete element method (DEM) to describe the fluid and the solid phases, respectively. The discharge rate of a large submerged granular sample is analyzed by varying orifice sizes and inter-particle cohesion strengths. For the submerged cohesionless case, we first study the revisited Beverloo relationship that includes the terminal velocity of a single falling particle in the fluid, proposed in the experimental work of Wilson *et al.* (2014). We consistently take into account the interstitial fluid with an effective orifice size smaller than in the dry case. Then, the additional contribution of grain cohesion is examined. Our main finding is that the empirical prediction remains valid provided that the orifice cutoff increases with cohesion. Finally, the evolution of fluid pressure during the discharge, at the vicinity of the orifice, is studied and favorably compared with the recent experimental study of Guo *et al.* (2017). By considering the pressure drop around the orifice as a driven-term, we succeed in predicting the solid flow rate with a similar Beverloo approach.

Keywords Granular flow · cohesive soil · solid discharge rate · DEM-LBM · hydro-mechanical modeling · sinkhole

Jianhua Fan, Gildas Noury
BRGM (French Geological Survey), DRP (Risk and Prevention), 3 avenue Claude Guillemin BP 36009, Orléans, 45060, France
E-mail: jianhua_fan@163.com

Li-Hua Luu, Pierre Philippe
Irstea, Aix Marseille Univ, RECOVER, 3275 Route de Cézanne, 13182 Aix-en-Provence, France

1 Introduction

The gravitational flow of granular media through an aperture has been the subject of many studies for hopper and hourglass problems [1,2], but much less with regard to geophysical processes such as soil subsidence and subsequent sinkhole formations related to the phenomenon of soil erosion [4,5]. The effects of climate change will probably drastically increase the occurrence of floods, but our knowledge of the hydro-mechanical instabilities of soil responsible for sinkhole occurrences is still poor and therefore insufficient to perform efficient risk assessments. In this paper, we focus on the collapse of cohesive soil layers above existing underground karst conduits in saturated situations after a flood. Since the underground process remains invisible from the surface, we here propose a simplified model that numerically simulates a submerged assembly of cohesive particles flowing through an orifice under the sole action of gravity.

Accurate prediction of discharge rates is crucial to address this issue. Depending on the orifice size and considering dry and cohesionless materials, three regimes of granular discharge are generally observed: a continuous flow, an intermittent flow, and the complete blockage of the flow due to arching. In the continuous flow regime, the mass flow rate $\dot{M}_s$ with a circular orifice can

be predicted empirically by the widely adopted Beverloo law (1961) [1]:

$$\dot{M}_s = C\rho_s\sqrt{g}(D-kd)^{\mathrm{Dim}-1/2} \quad (1)$$

where ρ_s is the solid density, g the acceleration of gravity, D the orifice size and d the grain diameter, while C and k are empirical coefficients for the two-dimensional case Dim = 2 and for the three-dimensional case Dim = 3, respectively. This relationship can be understood by considering two physical phenomena. First, it is assumed that the mechanism underlying the evacuation of grains is associated with the rupture of arches formed above the orifice [7]. Thus, the flow is calculated from the terminal free fall velocity of a particle in the air over a height D, defined by $\sqrt{gD}$, and the orifice section D^2. Then, the term $D - kd$ is used to define an apparent orifice size that accounts for the influence of a layer of grains close to the orifice edges where there is little or no motion. Values of k are found empirically and depend on grain shapes and size dispersion as well as inter-granular friction coefficients. For instance, the usual value for spherical particles is $k = 1.5$ [8], for sand it is $k = 2.9$ [1], while for air bubbles $k = 0.66$ has been reported [9]. Coefficient C is also slightly dependent on the coefficient of friction between grains and found to be in the range of $0.55 < C < 0.95$ [10]. The dry discharge rate through an orifice has been found to follow the Beverloo law for $D/d \geq 6$ [2,11,12]. Below this critical value, the flow is intermittent, causing jamming to occur [13].

Although the Beverloo law is supported by a considerable number of numerical and experimental works including [3,10–12,14,15], it has nevertheless been called into question since the experimental study of Janda *et al.* (2012) [16]. The classical interpretation in terms of apparent orifice appears to contradict the highlighting of self-similarity for the density and velocity profiles in the flow of particles through an aperture [16,18,17]. In the present work, we will however remain within the framework of the Beverloo law, which is mainly studied for dry non-cohesive granular material and mostly ignores the influence of the ambient fluid.

Relatively little research has been dedicated to submerged granular flows. Among the key experimental works, Wilson *et al.* [8] proposed a revision of the Beverloo law by describing the discharge rate with the terminal falling velocity of an individual grain in the fluid v_t, such that:

$$\dot{M}_s = C\rho_s v_t(D-kd)^{\mathrm{Dim}-1} \quad (2)$$

The main finding of these experiments was the increase of the coefficient k in the apparent orifice size due to the presence of the interstitial fluid. Further investigations focused, experimentally and numerically, on fluid-grain coupling [19,20]. The authors notably observed a surprising surge in the flow rate at the end of the hopper emptying process due to a non-constant pressure gradient. They pointed out the importance of examining the fluid pressure and velocity fields. Recently, Guo *et al.* [21] investigated water-submerged granular materials experimentally through a long efflux tube, by monitoring pressure variations with transducers. Their results were well-predicted by the forced solid flow model proposed by [2,22], that includes the following fluid pressure driven-term:

$$\dot{M}_s = C_s\phi\sqrt{\frac{P_2-P_1}{\rho_s}}d^2[D/d-k]^{\mathrm{Dim}-1} \quad (3)$$

where P_2 and P_1 are the pressures above and below the orifice respectively, and ϕ is the solid fraction.

On the other hand, numerous studies account for cohesion in granular flows, with applications in various industries ranging from food, pharmaceuticals, agriculture and mining, linked to fields of research such as powder aggregation [23,24], soil rheology [25] and rock mechanics [26]. Returning to our initial motivation to model cohesive soil destabilization, we are interested in internal attractive forces between particles that must be distinguished from macroscopic cohesion defined in a failure criterion of the Mohr-Coulomb type. We can roughly distinguish two types of inter-particle bonds, either formed by solid bridges (irreversibility) or liquid capillary-like bridges (reversibility). In this work in relation to erosion processes, we aim to model cohesive materials such as cemented calcareous sands for which different local models are proposed in terms of a contact law and a failure criterion [27,28].

This paper deals with submerged and cohesive granular flows through an aperture in connection with the phenomenon of the hydrostatic collapse of soil layers over underground cavity networks [4,5]. The DEM-LBM 2D-coupled numerical method is first introduced in Section 2. Then, simulation results for a parametric study (orifice size and cohesion strengths) of the solid discharge rate are presented in Section 3 with a thorough examination of the fluid flow (velocity and pressure) generated by the granular discharge. The conclusion and outlook for future work are finally presented in Section 4.

2 Numerical model

Compared with experimental studies, numerical simulations provide a more versatile and efficient way of investigating a wider range of variables. Such variables can be easily controlled, contrary to experiments in which some of them are barely measurable, such as the soil microstructural quantities and hydrodynamic parameters inside the system. Over the last decade, an increasing number of schemes that couple computational fluid dynamics (CFD) and the discrete element method (DEM) have been developed for treating the fluid-grain interactions involved in many complex geomechanical phenomena [29–34]. Relying on previous works, LBM-DEM that combines the lattice Boltzmann method for describing the fluid phase and the discrete element method for the solid phase, appears to be a highly efficient strategy for studying erosion processes, giving direct access to internal physical mechanisms [31]. The lattice Boltzmann method (LBM) indeed is an efficient alternative to classical CFD methods for simulating solid-fluid flows due to its intrinsic parallelism and capability of dealing with complex boundary conditions [35]. Furthermore, the discrete element method (DEM) has become a common approach for studying granular flows such as discharges through apertures [17,10,20] and through slit dams [36]. An increasing number of DEM models include inter-particle cohesive forces in the contact equation to describe cohesive granular materials [27,37,38]. This section is dedicated to a brief description of the DEM-LBM coupling method and is completed in the appendices.

2.1 Lattice Boltzmann Method for the fluid phase

The LBM is based on the Boltzmann equation [39] and derived from lattice gas cellular automata models. Generally, the computational domain in LBM is discretized by a number of nodes on a regular lattice and the fluid phase is assumed to be a group of fluid particles located at each lattice node. The state of the fluid particles is described by a distribution function $f_i(\mathbf{x},t)$ which indicates, at time t, the probability of fluid particles moving with velocity $\mathbf{e_i}$ along the ith direction of the node located at position $\mathbf{x}$.

For the present study, we employ the widely used and classical D2Q9 scheme that represents nine discrete velocities in a two-dimensional square lattice, as shown in Fig.1. The discrete velocities in the D2Q9 model are given by:

$$\mathbf{e}_i = \begin{cases} (0,0) & (i=0) \\ c(\cos\dfrac{\pi(i-1)}{2}, \sin\dfrac{\pi(i-1)}{2}) & (i=1,....4) \\ \sqrt{2}c(\cos\dfrac{\pi(2i-9)}{4}, \sin\dfrac{\pi(2i-9)}{4}) & (i=5,....8) \end{cases} \tag{4}$$

in which c stands for the lattice speed defined as:

$$c = h/\Delta t \tag{5}$$

where h is the lattice spacing and Δt is the time step.

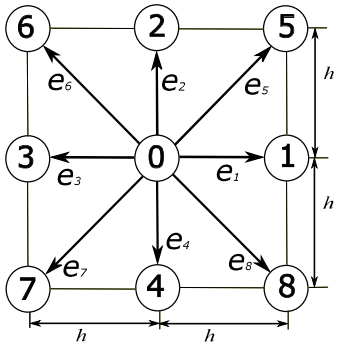

Fig. 1: Discrete velocity in the D2Q9 model

The time evolution of the density distribution function $f_i(\mathbf{x},t)$ in LBM is obtained by solving the following discrete form of the Boltzmann equation:

$$f_i(\mathbf{x}+\mathbf{e_i}t, t+\Delta t) - f_i(\mathbf{x},t) = \Omega_i(f) \tag{6}$$

which involves two successive sub-steps, namely collision and propagation steps

$$f_i(\mathbf{x},t^\star) = f_i(\mathbf{x},t) + \Omega_i(f) \tag{7}$$

$$f_i(\mathbf{x}+\mathbf{e_i}t, t+\Delta t) = f_i(\mathbf{x},t^\star) \tag{8}$$

where $f_i(\mathbf{x},t^\star)$ is called post-collision term and $t^\star$ is an intermediate time in the range $t < t^\star < t+\Delta t$. $\Omega_i(f)$ denotes the corresponding collision operator. The most widely used and simplest collision operator is the linearized Bhatnagar-Gross-Krook operator (called BGK) introduced by Bhatnagar et al. [40]. In this model, the density distribution function $f_i(\mathbf{x},t)$ tends to evolve towards equilibrium with a single relaxation time τ:

$$\Omega_i^{BGK} = -\frac{1}{\tau}(f_i(\mathbf{x},t) - f_i^{eq}(\mathbf{x},t)) \tag{9}$$

where the equilibrium distribution function f^{eq} reads:

$$f_i^{eq}(\mathbf{x},t) = w_i\rho_f(1+\frac{3}{c^2}\mathbf{e}_i\cdot\mathbf{u}+\frac{9}{2c^4}(\mathbf{e}_i\cdot\mathbf{u})^2-\frac{3}{2c^2}\mathbf{u}\cdot\mathbf{u}) \tag{10}$$

in which the weighting factors w_i depend on the model. For the D2Q9 model, $w_0 = \frac{4}{9}$, $w_{1,2,3,4} = \frac{1}{9}$, and $w_{5,6,7,8} = \frac{1}{36}$.

The macroscopic hydrodynamic variables at each lattice node, such as density ρ_f and velocity $\mathbf{u}$, can be evaluated from the particle distribution function as follows:

$$\rho_f = \sum_{i=0}^{8} f_i \tag{11}$$

$$\mathbf{u} = \frac{1}{\rho_f}\sum_{i=0}^{8} f_i\mathbf{e_i} \tag{12}$$

The fluid pressure p is directly determined by the following state equation:

$$p = c_s^2\rho \tag{13}$$

where c_s is the sound speed, defined as $c_s = \frac{c}{\sqrt{3}}$.

Finally, the kinematic viscosity ν is related to the lattice velocity c, the dimensionless relaxation time τ and the lattice spacing h through the following expression:

$$\tau = \frac{3\nu}{ch} + \frac{1}{2} \tag{14}$$

Since it has been proved that the macroscopic variables converge to the solution of Navier-Stokes equations through Chapman-Enskog expansion [41], the evaluation of incompressibility can be addressed by using the Mach number, defined by:

$$M_a = u_{max}/c \tag{15}$$

with u_{max} being the maximum simulated velocity in the flow. As the fluid in the LBM is assumed to be slightly compressible, M_a should keep a low value $M_a \ll 1$ during the simulations to recover an incompressible flow. A lattice speed c sufficiently higher than maximum velocity is required to ensure a reasonable solution. In practice, the low Mach number limit $M_a \leq 0.1$ should be satisfied.

However, the BGK model is based on a single relaxation time τ and therefore all the dynamic variables are dependent on the same dimensionless parameter. This deficiency probably leads to numerical instability problems when the relaxation time τ is close to 1/2. To overcome this problem, there are several alternative collision models in the literature, such as two-relaxation-time (TRT) and multiple-relaxation-time (MRT) operators. In this work, we employ the TRT model to relax the density distribution function, which avoids the numerical instabilities caused by the single-relaxation-time (SRT) model, and has the advantage of simplicity in comparison to the MRT method [42]. More specifically, the density distribution function is now decomposed into symmetric and antisymmetric parts:

$$f_i = f_i^+ + f_i^- \tag{16}$$

where f_i^+ and f_i^- are:

$$f_i^+ = \frac{f_i + f_{-i}}{2}, \qquad f_i^- = \frac{f_i - f_{-i}}{2} \tag{17}$$

with $-i$ being the notation for the vector $\mathbf{e}_{-i}$ that points in the opposite direction of $\mathbf{e}_i$ ($\mathbf{e}_{-i} = -\mathbf{e}_i$). The same process can be applied for the equilibrium particle distribution function resulting in:

$$f_i^{eq+} = \frac{f_i^{eq} + f_{-i}^{eq}}{2}, \qquad f_i^{eq-} = \frac{f_i^{eq} - f_{-i}^{eq}}{2} \tag{18}$$

In the TRT model, the evolution of the collision operator becomes

$$\Omega_i^{TRT} = \frac{1}{\tau^+}(f_i^+ - f_i^{eq+}) - \frac{1}{\tau^-}(f_i^- - f_i^{eq-}) \tag{19}$$

where τ^+ and τ^- are the symmetric and antisymmetric relaxation times. τ^+ controls the kinematic viscosity via $\nu = \frac{1}{3}(\tau^+ - \frac{1}{2})hc$, while τ^- is a free parameter often determined by a so-called magic parameter $\wedge$ that characterizes the stability properties of the TRT framework [43]: $\wedge = \left(\tau^+ - \frac{1}{2}\right)\left(\tau^- - \frac{1}{2}\right)$. An optimal value of $\wedge = \frac{1}{4}$ is provided to ensure stable simulations. Note that the BGK model [40] can be recovered from TRT when $\tau^+ = \tau^- = \tau$.

For the fluid-grain boundary condition, the partially saturated method (PSM) is implemented in the LBM algorithm. It deals with fluid-grain interaction by using a term that depends on the percentage of the cell saturated with fluid. More details are presented in Appendix A.

2.2 Discrete Element Method for the solid phase

DEM is an effective numerical method used to solve complex problems in solid mechanics, initially developed by Cundall and Strack in the 1970s [44]. The material is considered as an assembly of separate, discrete particles that interact through contact forces. The two force components, normal and tangential, are given by a viscoelastic Kelvin-Voigt model and a viscous-regularized Coulomb law, respectively. We also implement an interaction moment M, defined by the tangential force with the particles' radii as lever arms. A detailed description of the contact model is given in Appendix B.

For the analysis of the inter-granular cohesion, all the grains initially in contact are assumed to be bonded by a set of solid bridges with an elastic rheology characterized by normal and shear bond stiffness. Two models, proposed by Delenne et al. [27] and Silvani et al. [28], respectively, are combined to define the rheology of the cohesive zone. The first model is an elastoplastic model with a paraboloid yield surface in the space of the contact forces and torque. This model supplies the contact rheology, controlled by the relevant bond parameters (i.e. Kelvin-Voigt model) as long as the interaction forces remain within the yield volume. Once the yield value is reached, the contact is lost and the cohesive bond is definitively broken. As a result, the contact becomes purely frictional. The second model is a damage model that conveniently defines a damage zone within the yield volume, which involves a progressive degradation of the cohesive bond subjected to subcritical stresses. Finally, the combination of yield and damage surfaces provides the limits of the interaction force region. The rupture of the cohesive bond occurs instantaneously outside the yield domain while there is no bond degradation within the damage domain. In this model, for the sake of simplicity, the normal, shear and bending yield thresholds are assumed to depend on a unique force F_{coh} which represents the mean inter-particle bond strength. More details about this DEM cohesion model are given elsewhere [33].

2.3 Coupled LBM-DEM for fluid-solid interaction

The coupling between LBM and DEM is based on the sub-cycling time integration technique. Two time steps, Δt for fluid and Δt_{DEM} for particles, are used in the coupled procedure. In practice, the time step for fluid computation is larger than that for particle dynamics. Thus $\Delta t'_{DEM}$ is chosen according to the following equation:

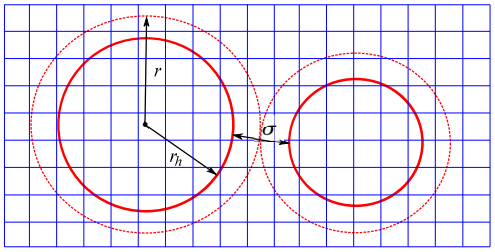

Fig. 2: Illustration of the hydraulic radius for the LBM and the grain radius for the DEM.

$$\Delta t'_{DEM} = \frac{\Delta t}{n_s} \tag{20}$$

where n_s is an integer greater than or equal to $\Delta t/\Delta t_{DEM}$. It is important to note that the reduced DEM time step here should be smaller than the critical time step (see Appendix B). Thus, one computational step of LBM includes n_s substeps of DEM time integration. Since the hydrodynamic forces and torques obtained with LBM remain unchanged during DEM subcycles, n_s should be selected as a small value for updating particle information. In the present model, n_s is restricted to 1 for each LBM step without altering DEM-LBM coupling, as discussed in Lominé *et al.* [29].

In 2D modeling, the solid disks in contact with each other can cause the unphysical situation where no fluid flows through the granular sample. In order to avoid this problem, a hydraulic radius approach is implemented in the LBM algorithm, where the solid grains are assumed to have a reduced radius r_h in the LBM calculation, while keeping the real grain radius r in the DEM loop (see Fig.2). A reasonable value of the ratio r_h/r is chosen equal to 0.8, as recommended by Cui *et al.* [45]. Consequently, we obtain a non-zero permeability in a 2D granular configuration.

3 Simulations of granular flows through an orifice

3.1 Numerical model setup

The evacuation of submerged grains through an aperture is simulated by the 2D DEM-LBM modeling described in the previous section. We use an adapted version of in-house codes previously developed by our research team and validated by two classical benchmark problems for micromechanical fluid-solid interaction, namely the drag coefficient of a single settling

particle and the sedimentation trajectories of a pair of grains [31,33]. All the simulation parameters for fluid and solid particles are listed in Table 1.

The computational domain consists of a fully saturated granular assembly at the bottom of which an orifice allows the grains to escape through an underground conduit, as presented in Fig.3. We implemented two different granular samples composed of 14857 and 15422 grains, whose mean diameter is $d = 4$ mm and $d = 2$ mm, respectively. As presented in the introduction, one key parameter of our study is the terminal velocity v_t, notably involved in Eq. 2, which v_t depends on the fluid and grain properties. It scales with the grain diameter as d^2 for the viscous (or Stokes) flow regime (low Re) and as $d^{1/2}$ for the fully inertial and turbulent regime (high Re) [8,46]. We determined v_t from separate DEM-LBM simulations of an isolated grain falling into a fluid, with the same grain and fluid parameters (Table 2). The flow regime is given by the particle Reynolds number defined as $Re = \frac{v_t d}{\nu}$, where $\nu = 10^{-4}$ m^2/s is the fluid kinematic viscosity. We choose here a viscosity substantially higher than that of water in order to limit the magnitude of the fluid velocity. Indeed, our LBM code is valid for incompressible flows (low Mach numbers, see Eq. (15)). Consequently, we were restricted to the laminar regime with low Reynolds numbers and with low Stokes numbers, defined as $St = \frac{\rho_s d^2}{18\rho_f \nu}\sqrt{\frac{(\rho_s-\rho_f)g}{2\rho_s d}}$, belonging to the so-called viscous regime [46,47] (Table 2).

The inter-particle cohesion of the sample is characterized by a dimensionless Cohesion number (at the particle scale) defined as the ratio of the bond strength F_{coh} to the particle's own buoyant weight:

$$Coh = \frac{F_{coh}}{(\rho_s - \rho_f)gS} \tag{21}$$

where $(\rho_s - \rho_f)$ represents the submerged apparent density and S is the particle's area (2D model). The gravitational flow is obtained in hydrostatic conditions, by setting the pressure at the surface and at the outlet of the conduit to zero. The grains within one diameter to the lateral and bottom walls are fixed and the boundary conditions are thus rough enough to prevent grain sliding. We propose a parametric study by varying (i) the size of the orifice D, from 10 to 90 times the diameter of the grain d, and (ii) the Cohesion number Coh, from 0 to 300.

Generally, the number of grains considerably affects the simulation time. In particular, a system composed of around 15000 grains requires a fairly high computational cost to simulate the entire flow process. Therefore, graphic processor units (GPU) are used with a parallelized version of our LBM-DEM code [33]. Thus, the current code makes it possible to simulate 1 second granular discharge using 45 minutes calculation time.

Table 1: Parameters of the DEM-LBM simulations

Solid phase	value	unit
Friction coefficient, μ	0.2	
Rolling friction coefficient, μ_r	0.1	
Bond strength, F_{coh}	0-56	N
Grain density, ρ_s	2.5×10^{-3}	kg/m^3
Normal stiffness, k_n	1.1×10^5	N/m
Tangential stiffness, k_t	1.1×10^5	N/m
Rolling stiffness, k_r	1.1×10^4	N/m
Coefficient of restitution, e_n	0.2	
Fluid phase		
Nb of horizontal nodes, l_x	1118	
Nb of vertical nodes, l_y	1600	
Fluid density, ρ_f	10^3	kg/m^3
Kinematic viscosity, ν	10^{-4}	m^2/s

Table 2: Granular sample characteristics: grain diameter d, sample height H, sample length L, terminal velocity v_t, particle Reynolds number Re, and Stokes number St.

d (cm)	H (cm)	L (cm)	v_t (m/s)	Re	St
0.2	25.5	22.4	0.07	1.45	0.21
0.4	50.0	44.5	0.16	6.40	0.60

3.2 Phenomenology

Fig. 3 shows snapshots of a typical simulation of a submerged granular discharge process for the cohesionless case. The submerged grains start to flow under the action of gravity and involve interstitial fluid entrainment. We observe a symmetrical concave profile at the surface of the grain sample packing. The fluid velocity field reveals an acceleration at the outlet, consistent with the conservation of the fluid flow rate through a significant section reduction. At the end of the discharge, dead zones are formed in the two bottom corners.

Regarding the cohesive submerged grains presented in Fig.4, we show the evolution of the intergranular bonds during the discharge process for three increasing Cohesion numbers, namely Coh=100, 150, and 300. Note that the single particles (after the rupture of all the bonds) are no longer visible in this kind of visualization that focuses on the occurrence of fractures.

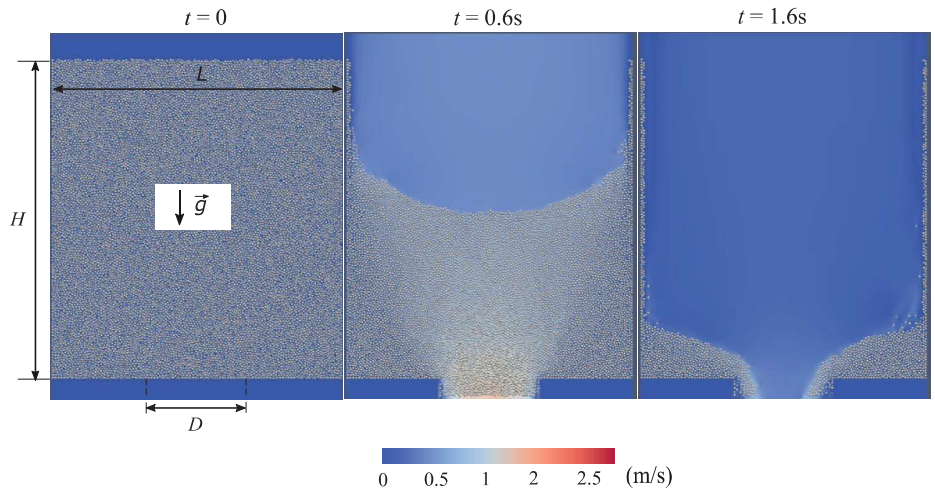

Fig. 3: Submerged granular discharge flow for a sample with 14857 cohesionless grains of mean diameter $d = 4$ mm, with $L = 44.5$ cm, $H = 50$ cm and $D/d = 40$. The color scale indicates the fluid velocity.

The bonds of the grains located at the lateral sides and at the orifice are much more easily broken than in the bulk, where the frictional influence of the wall is lower. Consequently, the granular top surface is no longer concave but remains almost horizontal because the grains at the surface are still bonded. The clusters formed above the outlet get larger with increasing cohesion. The second aspect displayed here is the kinetics of the discharge given by the time indication. As expected, cohesion progressively slows down the discharge rate. Finally, when further increasing inter-particle cohesion, we can observe the formation of a stable cavity resulting from the jamming of the granular flows. This is a significant example of arching built on the orifice edges, recalling the so-called intermittent discharge and complete blockage in the classical dry hopper problem [13].

3.3 Analysis of discharge rate

3.3.1 Methodology

Fig.5 presents the way we study the granular discharge quantitatively and parametrically, by counting the number of grains Nb escaping from the orifice as a function of time for different Cohesion numbers Coh and orifice sizes D. For the sake of readability, we display only certain representative cases. For all the curves, we observe that the number of eroded grains first increases monotonously. The larger the orifice, the higher the slope. Then, the rate gradually slows down to reach asymptotic behavior, corresponding to complete emptying. When adding cohesion, the same global evolution is displayed. Fluctuations occur as cohesion increases. This is probably related to the existence around the outlet of aggregates whose size seems to enhance with Coh, as depicted in Fig.4. Another general reason for fluctuations could be the occurrence of transient jamming that results from dynamic arching effect in the granular matter. Typically, the inset in Fig.5b shows the discharge curve corresponding to such an intermittent regime for Coh=300. We can distinguish successive flow phases. In a future work, we intend to properly and quantitatively characterize the size distribution of the aggregates within the granular sample during erosion, and its dependency on cohesion and orifice size.

Fig.6 presents the typical temporal evolution of the instantaneous solid flow rate, obtained by numerical differentiation of the eroded grains number Nb. The different curves exhibit a maximum flow rate that is more or less marked. The latter is lower for d=4 mm than for d=2 mm. Other works have already reported this dependency on particle size linked to a drag force effect [20]. To characterize the process duration, we define t_1 and t_2 as the limits of the temporal domain where the solide discharge Q_s is larger than 10% of its maximal value, as sketched in Fig. 6. In the following analysis, we perform two different quantifications of the discharge rate. First, we consider the maximum value reached, denoted by Q_s^m. And secondly, we determine the average discharge rate between t_1 and t_2, denoted by $\bar{Q}_s$. The maximum discharge rate Q_s^m as a function of the average discharge rate $\bar{Q}_s$ is plotted in the inset of Fig.6 and highlights a quite linear correlation $Q_s^m = 1.5\bar{Q}_s$, showing that the two approaches are consistent.

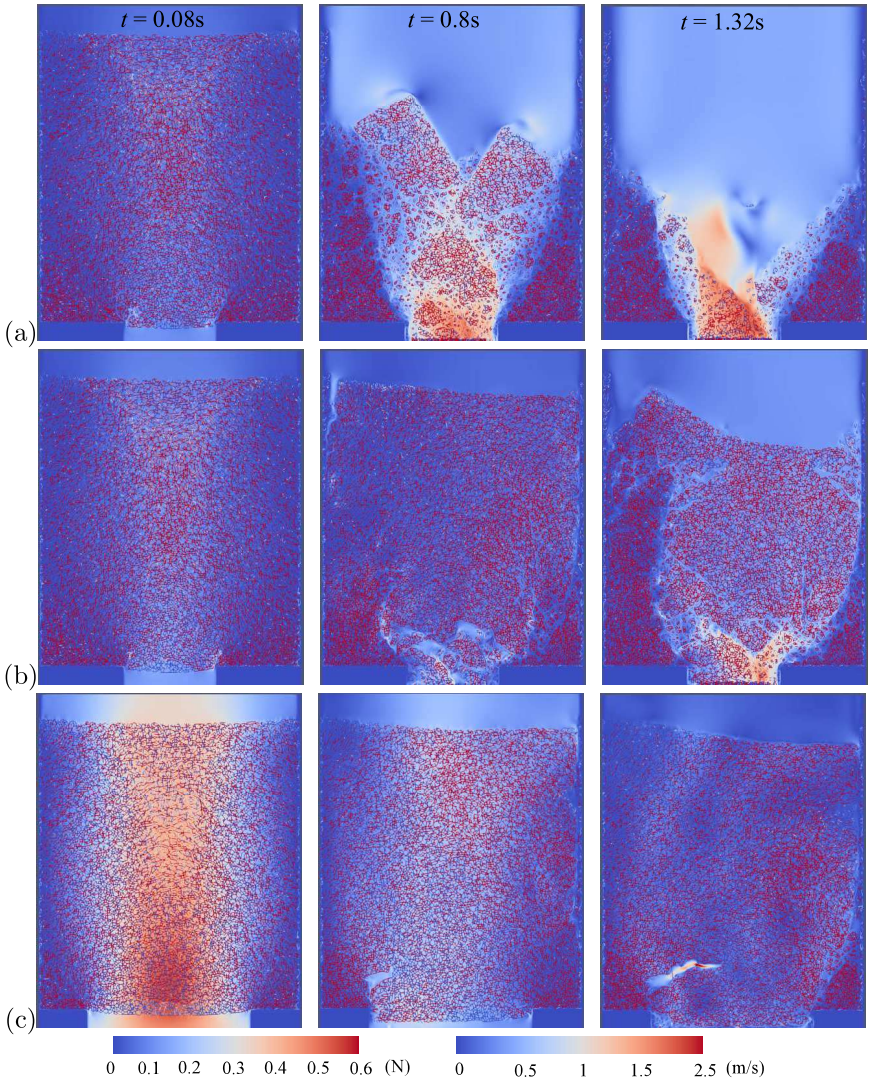

Fig. 4: Typical simulations for submerged cohesive granular discharge (a) $Coh = 100$ and $D/d = 40$, (b) $Coh = 150$ and $D/d = 40$, (b) $Coh = 300$ and $D/d = 70$. Visualization of the link between the centers of bonded particle pairs. The color scales indicate the fluid velocity and the inter-particle normal force.

3.3.2 Parametric study

The analysis of the granular flow that we propose is based on the Beverloo law presented in the introduction. For the classical dry case, it is assumed that the relationship given in Eq. (1) could explain the emptying of a hopper through successive ruptures of arches formed above the orifice [13]. Thus, the discharge rate is calculated according to the characteristic free-fall speed of a grain in air, defined by $\sqrt{gD}$. For the submerged granular flow, we have to introduce the interstitial fluid effect. To this end, an experimental work by Wilson *et al.* [8] proposed a modified Beverloo law that predicts the discharge rate from the terminal falling velocity of an individual grain in the fluid v_t, given in Eq. (2). The main finding of this experimental study was the increase of the coefficient k in the apparent orifice size due to the fluid-grain interaction.

For the present numerical model, we propose to transpose this adapted law from 3D (Dim=3) to 2D (Dim=2) by considering the solid mass flow rate $\dot{M_s}^{\mathrm{2D}}$ (in $\mathrm{kg.s^{-1}.m^{-1}}$), as follows:

$$\dot{M_s}^{\mathrm{2D}} = C'\rho_s v_t[D - kd] = C'\rho_s v_t d[D/d - k] \tag{22}$$

Knowing that $\dot{M_s}^{\mathrm{2D}} = Q_s(\rho_s \frac{\pi d^2}{4})$ with the solid flow rate $Q_s = \mathrm{d}Nb/\mathrm{d}t$ (in $\mathrm{s^{-1}}$), we can write:

$$Q_s = C'\frac{4}{\pi d}v_t[D/d - k] \tag{23}$$

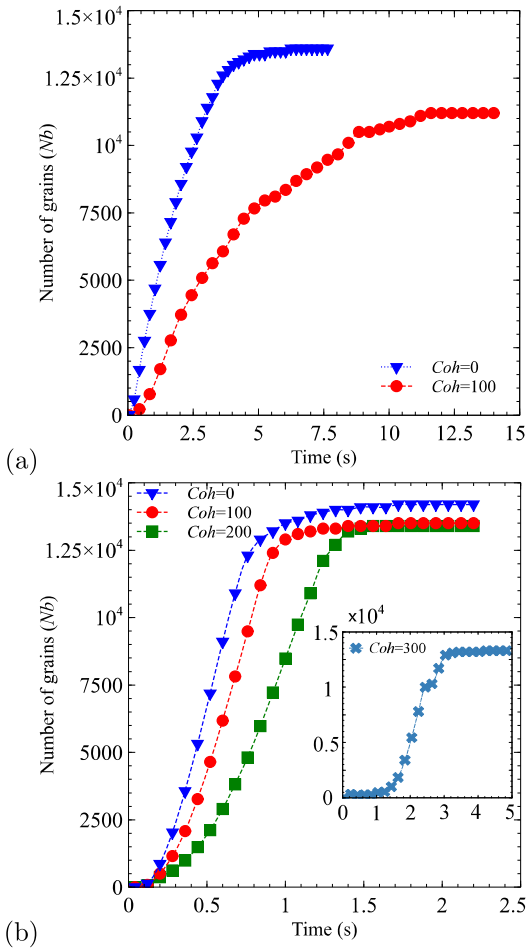

Fig. 5: Number of grains flowing through the orifice as a function of time for various Cohesion numbers Coh (for the granular sample with d=4 mm) (a) $D/d = 20$ and (b) $D/d = 70$.

For all the simulations, Fig.7a presents the maximum discharge rate Q_s^m normalized by $\frac{4v_t}{\pi d}$ *versus* the orifice size D normalized by the grain diameter d. The error bars come from an estimate of 90% confidence interval. Linear fits agree well with numerical data for both granular samples and for the different granular cohesion states. Without cohesion, the slope denoted by C' according to Eq. (23), is higher for the sample of d=2 mm ($C' = 11.4 \pm 0.2$) than d= 4 mm ($C' = 7.4 \pm 0.2$). Nevertheless, the Beverloo cutoff is the same, $k = 5.47 \pm 0.03$. As expected, this value is higher than the dry case, $k = 1$ in 2D-DEM simulations [15]. Adding the effect of an interstitial fluid indeed decreases the apparent orifice, as interpreted by Wilson *et al.* [8]. To reinforce this finding, we performed simulations with a dimensionless orifice diameter D/d=5 lower than the fitted value of k. For both granular samples, the expected

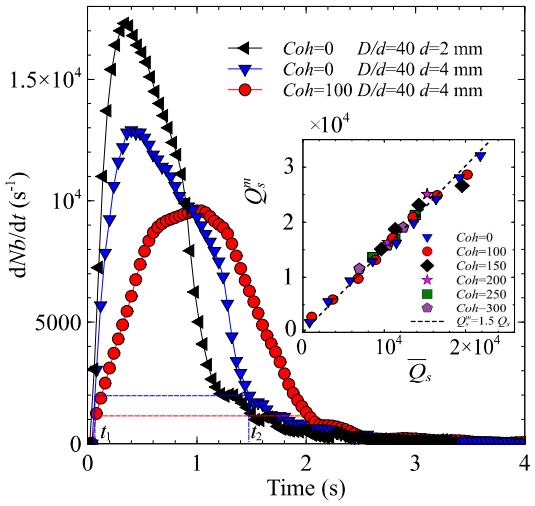

Fig. 6: Instantaneous discharge rate dNb/dt *versus* time. t_1 and t_2 represent the start and end time of the discharge. Inset: Q_s^m *versus* $\bar{Q}_s$ (for the granular sample with d=4 mm). The dotted line stands for $Q_s^m = 1.5\bar{Q}_s$

.

jamming occurred, thus ensuring consistency with the physical meaning of the Beverloo cutoff.

When adding cohesion, we still obtain satisfactory linear fits when fixing the same coefficient C' than the one fitted for the cohesionless case. It is noteworthy that there is no data for small D when Coh is high. In these conditions, the granular media does not necessarily jam but is subject to significant intermittent flows. This behavior distorts the present estimation of Q_s^m and therefore prevents data acquisition. Fig.7b shows the regular increase of k as a function of granular cohesion Coh. This trend is quite consistent with the numerical study of Anand *et al.* [37] who demonstrated, using DEM simulations of grains connected by capillary bridges, that k increases with the Bond number Bo, defined as the ratio of liquid surface tension to gravitational force acting on the particle, equivalent to Coh. Therefore, in addition to the interstitial fluid effect, the existence of bonds between the grains decreases the apparent orifice size even more. However, we remark that for a same Coh, k is lower when d is smaller. Further studies are needed to rationalize this outcome. Finally, the same analysis with $\bar{Q}_s$ instead of Q_s^m gives similar k values and evolution but with a systematic shift downwards, as shown in Fig.7b.

From the present simulations, we can also analyze the characteristic duration of the discharge process given by the time lag between t_1 and t_2: $t_D = t_2 - t_1$. The inset in Fig.8 shows typical plots of t_D as a function of D/d. As commented earlier, the larger the orifice size and/or the smaller the inter-particle cohesion, the

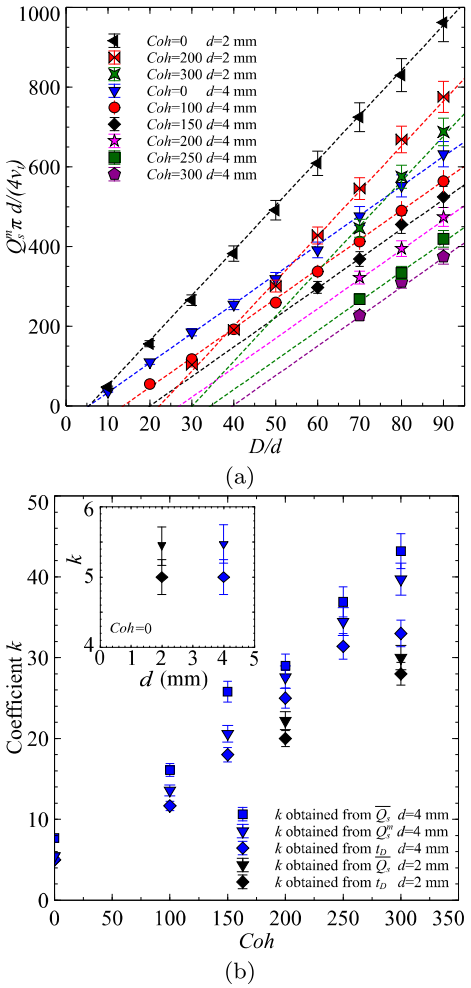

Fig. 7: (a) Maximum discharge rate Q_s^m scaled by $(4v_t/(\pi d))$ as a function of the dimensionless size of the orifice D/d for the two granular samples and for different Cohesion numbers Coh. Dashed lines indicate linear fits of Eq. (23) giving $C' = 11.4 \pm 0.2$ for d=2 mm, and $C' = 7.4 \pm 0.2$ for d=4 mm. (b) Coefficient k obtained from Q_s^m, $\bar{Q}_s$ and t_D analyzed as a function of Cohesion numbers Coh.

slower the discharge. Drawn from the previous scaling given by Eq. (23), we empirically found a good correlation between t_D and D/d when considering the following power-law relation $t_D \propto (D/d - k)^{-4/3}$. The corresponding prefactor is found to be the same for all granular samples (for a given diameter d and different cohesion numbers Coh). With the k values obtained from the latter fit, we plot $t_D^{-3/4}$ *versus* $(D/d - k)$ for our numerical data and consistently observe two separate collapses, according to the two different diameters d. As shown also in Fig.7b, the k values resulting from this analysis are lower than those deduced from Q_s^m and

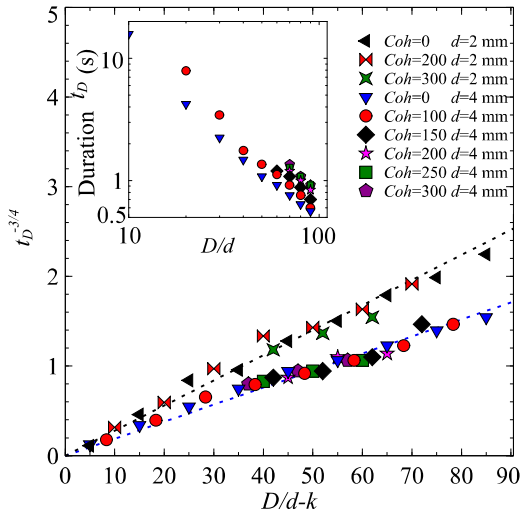

Fig. 8: Duration $t_D^{-3/4}$ as a function of $D/d - k$ for all simulations. The dotted lines stand for linear regressions (see text for details). Inset: t_D as a function of D/d for d=4 mm and various Coh (on a log-log scale).

$\bar{Q}_s$, but it displays the same monotonic increase with Coh.

3.4 Fluid flow during cohesionless solid discharge

In this last subsection, we propose to study to what extend the fluid flow in the vicinity of the orifice is related to the solid discharge rate. Whereas flow monitoring within a granular flow is difficult to perform experimentally, our simulations provide hydrodynamic quantities anywhere in the numerical domain. Here, we propose to look closer at the cohesionless case where the fluid flow can be properly acquired. We acquire the exact flow measurement (velocity and pressure) in purely fluid domains. In the presence of grains, as presented in Appendix A, the LBM code applies the PSM method at the solid interfaces and considers the DEM solid velocity at each node within the particles.

When the submerged grains move downwards by gravity, their motion entrains the interstitial fluid. The fluid velocity at the top boundary, where we impose a zero-pressure condition, varies according to the outlet flow by mass conservation. Fig. 9 shows the correlation between particle velocity and fluid velocity, as the discharge rate reaches its maximum. To obtain this, we select a temporal window corresponding to values of Q_s larger than 80% of Q_s^m. Then, for each time step of this selected part of the process, we determine a mean particle velocity U_s, defined by the x-average DEM velocity within the granular sample (at y =0.3 m for $10< D/d <40$ and y=0.5 m for $50< D/d <90$), and a

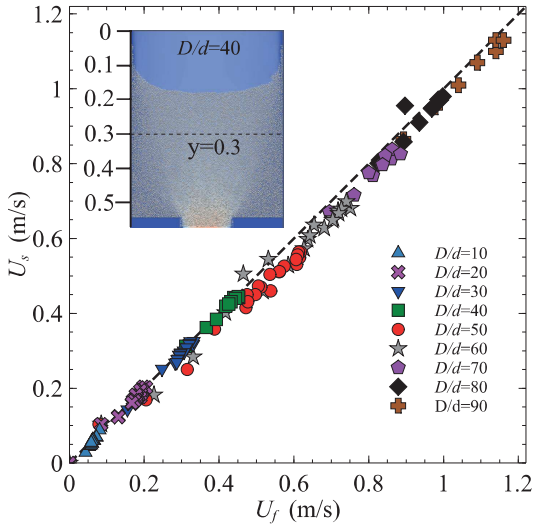

Fig. 9: Around the maximum discharge rate: mean particle velocities in the bulk U_s as a function of mean fluid velocities at the inlet U_f (for the granular sample with d=4 mm).

mean fluid velocity U_f, defined by the x-average LBM velocity at the inlet (at y=0). We observe a clear linear correlation with a slope close to 1. The fluid therefore flows passively downwards at the same speed as the grains, around the maximum discharge rate.

Fig. 10 presents typical fluid velocity and pressure profiles along the median line, from the surface to the end of the conduit (see the inset in Fig. 10a). Fig. 10a shows a fluid velocity that is constant above the granular sample and which increases slowly up to the outlet due to the sudden contraction of the flow section. In parallel, the pressure profile in Fig. 10b correspondingly exhibits a pressure drop around the orifice of the underground conduit. There is a positive maximum value P_{max} above the outlet and a negative minimum value P_{min} just below it. This result is corroborated by a recent experimental work conducted by Guo *et al.* (2017), in which the authors monitored pressure variations with transductors during a water-submerged granular flow through a long efflux tube [21]. Fig.11a shows the time evolution of P_{max} and P_{min} (which are systematically above and below the outlet, respectively) for different orifice sizes. Located above the outlet, P_{max} displays a maximum followed by a decrease in time while P_{min} behaves almost symmetrically with negative values. These features are in full qualitative agreement with the experimental measurements reported previously [21].

As mentioned in the introduction section, in the field of powder technology, empirical laws have been proposed to model air-assisted granular flows through long tubes [2,22]. From these experimental studies, the

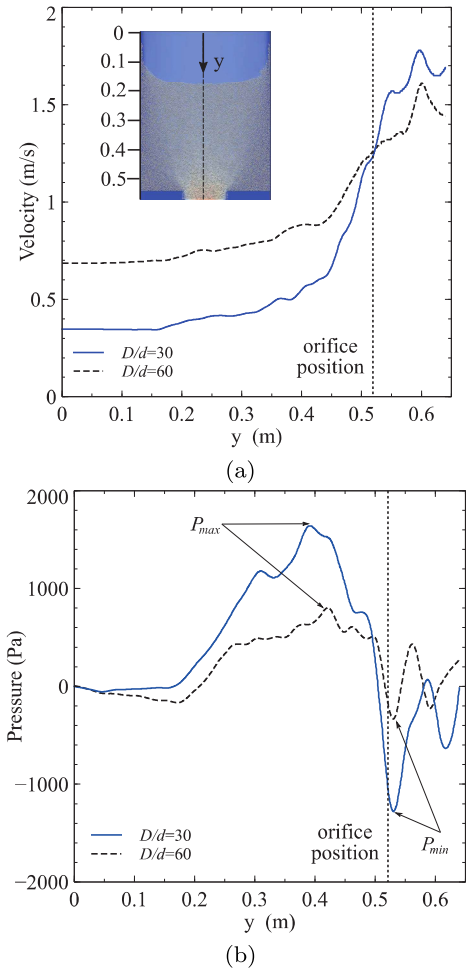

Fig. 10: Typical flow velocity (a) and pressure (b) profiles along the flow direction during the discharge. For the sake of readability, the curves have been smoothed *via* a loess method (span of 10%).

most usual relationship for the solid mass flow rate takes into account the effect of differential pressure, as written in Eq. (3). The term $(D/d - k)$ is related to the same concept of apparent orifice as advocated in the Beverloo laws. Fig.11b indeed shows the time evolutions of $\sqrt{\Delta P}$ that are qualitatively very similar to the grain discharge rate $\mathrm{d}Nb/\mathrm{d}t$ (Fig.6) and which depends on the orifice diameter D. The larger D/d, the smaller $\sqrt{\Delta P}$ becomes. In line with our previous analysis in section 3.3 and based on Eq. (3), we study the following 2D-adapted relationship for the solid flow rate expressed by number of particles per second (in s^{-1}):

$$Q_s = C'_s \phi \frac{4}{\pi d} \sqrt{\frac{P_2 - P_1}{\rho_s}} [D/d - k] \qquad (24)$$

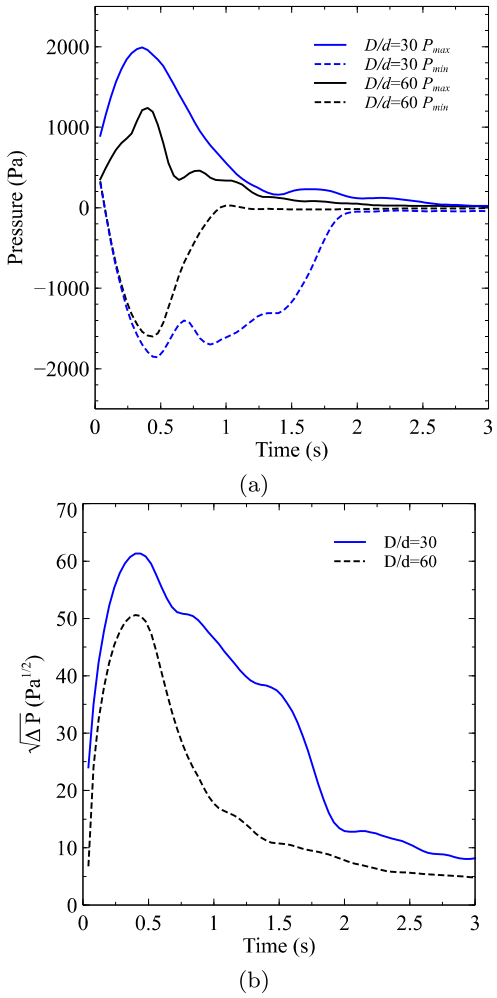

Fig. 11: Typical pressure evolution in time: (a) P_{min} and P_{max}. (b) $\sqrt{\Delta P} = \sqrt{P_{max} - P_{min}}$. For the sake of readability, the curves have been smoothed *via* a loess method (span of 10%).

We recover Eq.(2) in which the terminal velocity is replaced by a pressure drop term $\sqrt{\frac{P_2-P_1}{\rho_s}}$. To study this expression, we define the ratio R such that:

$$R = \frac{\mathrm{dNb/d}t}{\sqrt{\frac{P_2-P_1}{\rho_s}}\frac{\pi d}{4\phi}} \tag{25}$$

Note that the DEM solid fraction is equal to 0.83 for the both two samples. By taking into account the hydraulic radius r_h=0.8 (Fig. 2), we obtain $\phi = 0.83 r_h^2 = 0.53$. The inset of Fig. 12 presents a typical time evolution of the ratio R. Similar to the previous determination of Q_s^m, we average around the maximum to acquire the characteristic value R_m, as depicted in the inset. Finally, we plot R_m as a function of D/d for all orifice sizes and the two granular samples. All data gathers on a single curve that is linearly well fitted, to obtain $R_m = C_s'[D/d - k]$, with $C_s' = 2.3 \pm 0.1$ and $k = 9.3 \pm 2.6$. The value of the Beverloo-like cutoff k is higher but remains consistent with the previous analysis, that in contrast led to a coefficient C' dependent on the terminal velocity v_t. Here, the data collapse means that the pressure drop term contains the lacking physics, thus giving a more uniform law for the solid discharge rate. However, this pressure measurements is difficult to obtain in practice, whereas v_t can be calculated from analytical solutions [46].

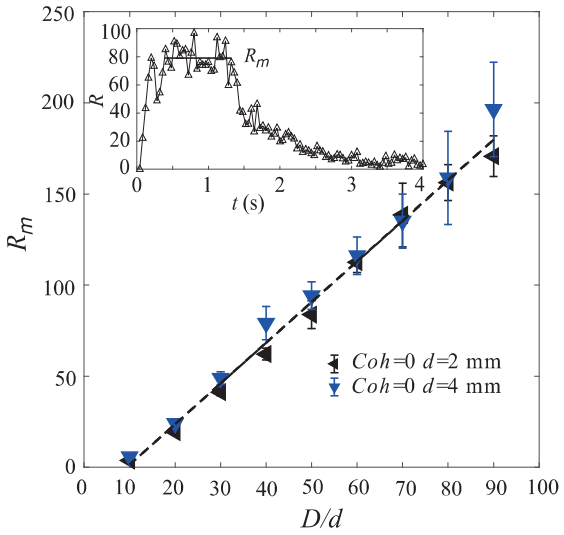

Fig. 12: R_m as a function of D/d for the two granular samples. Inset: typical time evolution of the ratio R and estimation of R_m for D/d=40.

4 Conclusion

In this article, we investigated the physical modeling of the hydro-mechanical process of cohesive submerged soil discharge through an underground orifice, notably applicable to sinkhole occurrences in a flooded situation. The numerical study was based on a coupled DEM-LBM method involving a cohesion DEM-model that allowed simulation on to the grain-fluid interaction scale during a gravitational granular flow discharge. A parametric investigation was carried out to study the influence of the cohesion of the granular medium and the size of the orifice D on the solid flow rate Q_s. Consistent with a adapted 2D-Beverloo law for a submerged hopper [8], we observed a linear increase of Q_s with the apparent orifice size $(D/d - k)$, that was found to be smaller than in the dry case. By adding inter-particle cohesion, the cutoff k increased even more. The higher the cohesion, the smaller the apparent orifice size. This

interpretation of particle cohesion agrees with a recent DEM study on capillary bonded, but non-saturated, granular discharge [37].

Using the LBM-fluid calculation, we studied the fluid flow generated downward by the motion of the particles. The systematic acquisition of the pressure drop around the orifice during discharge was performed. We obtain qualitative agreement with recent experimental measurements using transducers [21]. By replacing the terminal velocity term in the Beverloo-like law with a squared pressure drop term, all the data collapsed regardless of particle size. This new finding satisfactorily links the experimental works of Wilson *et al.* (2014) and Guo *et al.* (2017).

One of our immediate prospects is to now move from gravitational flow configuration to pressure-driven discharge. The work now in progress is focused more specifically on particle-fluid interaction, notably by considering drag force in the pressure analysis. To improve our understanding of soil cohesion, since this DEM-LBM method permits taking a micromechanical approach, we intend to systematically characterize the spatial and temporal size distribution of the aggregates. Another perspective will be to calibrate our numerical modeling with experiments on artificial cemented materials recently developed in our laboratory [48]. Beyond such hopper-like configurations, the present study of submerged cohesive granular flow aims at improving knowledge and understanding of complex covered-collapse sinkhole processes in karst terrains during or after a flood. [4,5].

Acknowledgements

This research was partly funded by PERCIVAL (PErception des Risques effondrements liés aux Cavités associés aux Inondations en VAL de Loire) French Regional Research Program (2018-2020) attributed by the Centre-Val de Loire region.

Appendix A: Partial Saturation Method (PSM)

The Partially Saturated Method (PSM) was originally developed by Noble and Torczynski [49] to consider a modified non-slip condition. A virtual lattice cell, associated with each lattice node, can be completely or partially saturated depending on the solid fraction, as sketched in Fig.13. Then it gives:

$$f_i(\mathbf{x}+\mathbf{e_i}t, t+\Delta t) = f_i(\mathbf{x},t) - [1-B(\epsilon,\tau)]\Omega_i^{TRT} + B(\epsilon,\tau)\Omega_i^s \quad (26)$$

where Ω_i^{TRT} accounts for fluid particle collisions at the same node and Ω_i^s describes the interactions with solid particles within the computational lattice. $B(\epsilon,\tau)$ is a weighting function defined as:

$$B(\epsilon,\tau) = \frac{\epsilon(\tau-1/2)}{(1-\epsilon)(\tau-1/2)} \quad (27)$$

where ϵ stands for the solid volume fraction on each lattice node $0 \leq \epsilon \leq 1$. $B(\epsilon=0,\tau)=0$ corresponds to a pure fluid whereas $B(\epsilon=0,\tau)=1$ denotes a pure solid. The collision operator Ω_i^s for solid nodes is based

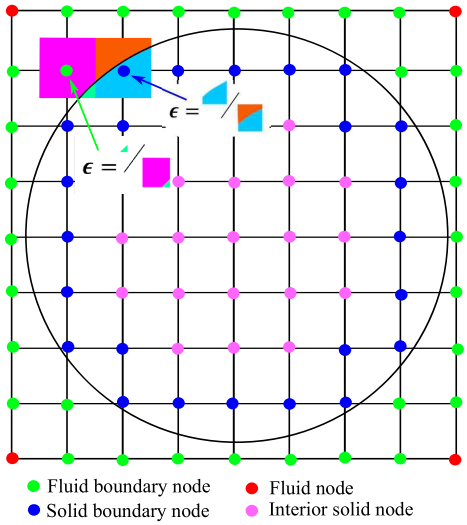

Fig. 13: Conceptual sketch of the Partial Saturation Method (PSM) involving the local solid volume fraction ϵ defined at each lattice node.

on the concept of the bounce-back [50] of the density function distribution given by [49]:

$$\Omega_i^s = f_{-i}(\mathbf{x},t) - f_i(\mathbf{x},t) + f_i^{eq}(\rho_f, \mathbf{u}_s) - f_{-i}^{eq}(\rho_f, \mathbf{u}) \quad (28)$$

where $\mathbf{u}_s$ is the velocity of solid particles. Regarding the fluid-wall boundary condition, since the pressure and velocity derived from the density distribution functions f_i cannot be imposed directly on the boundaries, a simple boundary condition method proposed by Zou and He [50] is applied on the system. This method involves the bounce-back of the non-equilibrium part of the density distribution functions at the boundary. The hydrodynamic force and torque applied on a solid obstacle can be determined from:

$$\mathbf{F}^h = \frac{(\Delta x)^{\mathrm{Dim}}}{\Delta t} \sum_n B_n \sum_i \Omega_i^s \mathbf{e}_i \quad (29)$$

$$\mathbf{T}^h = \frac{(\Delta x)^{\mathrm{Dim}}}{\Delta t} \sum_n B_n (\mathbf{x}_i - \mathbf{x}_s) \times \sum_i \Omega_i^s \mathbf{e}_i \quad (30)$$

where, here, Dim again denotes dimension (Dim = 2 for 2D case). B_n stands for the B value at node n, which represents all the lattice nodes occupied by the solid. $\mathbf{x}_s$ is the center of mass of the solid obstacle.

Appendix B: DEM contact model

In DEM, some simple geometrical objects such as circular disks, spheres and squares are considered as discrete particles. Each particle has its own mass, velocity and contact properties, while its motion is based on Newton's second law. Each solid particle is driven by a total contact force $\mathbf{F}_i^c$, which is equal to the summation of the contact forces over all the interacting particles, a hydrodynamic force $\mathbf{F}_i^h$ resulting from the fluid action, and the gravitational force. At each DEM time step, the new position and velocity of a particle can be updated from the following explicit time integration:

$$m_i \frac{\mathrm{d}\mathbf{u}_i}{\mathrm{d}t} = \mathbf{F}_i^c + \mathbf{F}_i^h + m_i g \quad (\text{with} \quad \frac{\mathrm{d}\mathbf{x}_i}{\mathrm{d}t} = \mathbf{u}_i) \tag{31}$$

$$\mathbf{T}_i^c + \mathbf{T}_i^h = J\dot{\boldsymbol{\omega}} \tag{32}$$

where m_i, $\mathbf{x}_i$ and $\mathbf{u}_i$ are the particle mass, position and velocity, respectively. $\mathbf{T}_i^c$ and $\mathbf{T}_i^h$ are the torque resulting from the inter-particle contact forces and the fluid torque, respectively,. J is the moment of inertia and ω the angular velocity while g is gravity. The particle position and its velocity are solved using time integration with the Verlet algorithm.

When two circular particles i and j, located at positions $\mathbf{r_i}$ and $\mathbf{r_j}$, touch each other, their contact is allowed to slightly overlap:

$$\delta_{ij}^n = R_i + R_j - (\mathbf{r_i} - \mathbf{r_j}) \cdot \mathbf{n} > 0 \tag{33}$$

where R_i and R_j are the particle radii. The contact force $\mathbf{F}_{ij}^c$ between the two particles is given by:

$$\mathbf{F}_{ij}^c = F_{ij}^n \mathbf{n} + F_{ij}^t \mathbf{t} \tag{34}$$

where F_{ij}^n stands for the normal force and F_{ij}^t for the tangential force.

The normal component F_{ij}^n of the contact force is computed as:

$$F_{ij}^n = -k_n \delta_{ij}^n - \gamma_n v_{ij}^n \tag{35}$$

where k_n is the normal spring stiffness of the interaction and γ_n is the normal coefficient of viscous dissipation.

The tangential component of the contact force is calculated using a viscous-regularized Coulomb model [33]:

$$F_{ij}^t = -\min(k_t \delta_{ij}^t, \mu F_{ij}^n) sgn(\delta_{ij}^t) \tag{36}$$

where k_t is the coefficient of regularization and μ is the friction coefficient while δ_{ij}^t stands for the tangential spring deformation.

The mechanical torque defined by the tangential force with the particles' radii as lever arms is complemented by the following rolling resistance:

$$T_{ij}^{roll} = -\frac{\mathbf{v_r}}{\mid \mathbf{v_r} \mid} \mu_r F_{ij}^n R_{ij}^{eff} \tag{37}$$

where $\mathbf{v_r}$ is the rolling velocity defined by the difference of angular velocities between particles i and j. $R_{ij}^{eff} = \frac{R_i R_j}{R_i + R_j}$ denotes the effective radius and μ_r is the rolling coefficient.

The critical time step related to the period of oscillations at contact should be appropriately chosen in the Newton equations. In particular, the time step of the DEM Δt_{DEM} should be below the critical value Δt_{cr} corresponding to the mass-spring oscillator of the smallest particle mass m and stiffness k:

$$\Delta t_{cr} = 2\pi \sqrt{m/k_n} \tag{38}$$

To avoid any instability of the numerical method, a reasonable coefficient $\lambda = 0.1$ is selected between the DEM time step and this critical value: $\Delta t_{DEM} = \lambda \Delta t_{tr}$.

Note that the normal coefficient γ_n of viscous dissipation is related to the macroscopic coefficient of restitution e_n [51]:

$$\gamma_n = \frac{-2 \ln e_n \sqrt{m k_n}}{\sqrt{\pi^2 + \ln^2 e_n}} \tag{39}$$

References

1. Beverloo, W.A., Leniger, H.A., Van de Velde, J.: The flow of granular solids through orifices. Chem. Eng. Sci. 15, 260–269 (1961).
2. Nedderman, E.M., Tüzün, U., Savage, S.B., Houlsby, G.T.: The flow of granular materials-I Discharge rates from hoppers. Chem. Eng. Sci. 37, 1597–1609 (1982).
3. Langston, P. A., Tüzün, U., Heyes, D. M.: Discrete element simulation of granular flow in 2D and 3D hoppers: dependence of discharge rate and wall stress on particle interactions. Chem. Eng. Sci. 50(6), 967-987 (1995).
4. Luu, L., Philippe, P., Noury, G., Perrin, J., Brivois, O.: Erosion of cohesive soil layers above underground conduits. EPJ Web Confecrences. 09038, 3–6 (2017).

5. Luu, L.-H., Noury, G., Benseghier, Z., Philippe, P.: Hydro-mechanical modeling of sinkhole occurrence processes in covered karst terrains during a flood. Eng. Geol. 260, 105249 (2019).
6. Mankoc, C., Garcimartín, A., Zuriguel, I., Maza, D., Pugnaloni, L.: Role of vibrations in the jamming and unjamming of grains discharging from a silo. Phys. Rev. E 80(1), 011309 (2009).
7. To, K., Lai, P. Y., Pak, H. K. Jamming of granular flow in a two-dimensional hopper. Phys. Rev. E. 86(1), 71 (2001).
8. Wilson, T.J., Pfeifer, C.R., Meysingier, N., Durian, D.J.: Granular discharge rate for submerged hoppers. Pap. Phys. 1307, 2812 (2014).
9. Bertho, Y., Becco, C., Vandewalle, N.: Dense bubble flow in a silo : an unusual flow of a dispersed medium. (2007)
10. Anand, A., Curtis, J.S., Wassgren, C.R., Hancock, B.C., Ketterhagen, W.R.: Predicting discharge dynamics from a rectangular hopper using the discrete element method (DEM). Chem. Eng. Sci. 63, 5821–5830 (2008).
11. Hirshfeld, D., Radzyner, Y., Rapaport, D.C.: Molecular dynamics studies of granular flow through an aperture. Phys. Rev. E. 56, 4404–4415 (1997).
12. Hilton, J.E., Cleary, P.W.: Granular flow during hopper discharge. Phys. Rev. E. 011307, 1–10 (2011).
13. Zuriguel, I., Garcimartín, A., Maza, D., Pugnaloni, L. A., Pastor, J. M.: Jamming during the discharge of granular matter from a silo. Physical Review E, 71(5), 051303 (2005).
14. Lin, P., Zhang, S., Qi, J., Xing, Y.M., Yang, L.: Numerical study of free-fall arches in hopper flows. Physica A. 417, 29–40 (2015).
15. Choi, J., Kudrolli, A., Bazant, M.Z.: Velocity profile of granular flows inside silos and hoppers. J. Phys. Condens. Matter. 17, S2533–S2548 (2005).
16. Janda, A., Zuriguel, I., Maza, D.: Flow rate of particles through apertures obtained from self-similar density and velocity profiles. Physical review letters, 108(24), 248001 (2012).
17. Hu, G., Lin, P., Zhang, Y., Li, L., Yang, L., Chen, · Xiaosong: Size scaling relation of velocity field in granular flows and the Beverloo law. Granul. Matter. 21, 21 (2019).
18. Zhou, Y., Lagrée, P. Y., Popinet, S., Ruyer, P., Aussillous, P.: Experiments on, and discrete and continuum simulations of, the discharge of granular media from silos with a lateral orifice. Journal of Fluid Mechanics, 829, 459-485 (2017).
19. Koivisto, J., Durian, D.J.: The sands of time run faster near the end. Nat. Commun. 8, 15551 (2017).
20. Koivisto, J., Korhonen, M., Alava, M., Ortiz, C.P., Durian, D.J., Puisto, A.: Friction controls even submerged granular flows. Soft Matter. 13, 7657–7664 (2017).
21. Guo, S., Yu, T., Zhang, Y.: Water-submerged granular flow through a long efflux tube. Granul. Matter. 2–9 (2017).
22. Bulsara, P.U., Zenz, F.A., Eckert, R.A.: Pressure and additive effects on flow of bulk solids. Ind. Eng. Chem. Process Des. Dev. 3, 348–355 (1964).
23. Rumpf,H.: The Strength of Granules and Agglomerates, Interscience, New York, (1962).
24. Kendall, K., Stainton, C.: Adhesion and aggregation of fine particles. Powder Technol. 121, 223–229 (2001).
25. Mitchell,J. and Soga,K.: Fundamentals of soil behavior, Wiley, New York, (1976).
26. Jaeger, J.C., Cook, N.G. and Zimmerman, R.: Fundamentals of rock mechanics, John Wiley & Sons, (2009).
27. Delenne, J.Y., El Youssoufi, M.S., Cherblanc, F., Bénet, J.C.: Mechanical behaviour and failure of cohesive granular materials. Int. J. Numer. Anal. Methods Geomech. 28, 1577–1594 (2004).
28. Silvani, C., Désoyer, T., Bonelli, S.: Discrete modelling of time-dependent rockfill behaviour. Int. J. Numer. Anal. Methods Geomech. 33, 665–685 (2008).
29. Lominé, F., Scholtès, L., Sibille, L., Poullain, P.: Modeling of fluid-solid interaction in granular media with coupled lattice Boltzmann/discrete element methods: application to piping erosion. Int. J. Numer. Anal. Methods Geomech. 37, 577–596 (2013).
30. Tran, D. K., Prime, N., Froiio, F., Callari, C., Vincens, E.: Numerical modelling of backward front propagation in piping erosion by DEM-LBM coupling. European Journal of Environmental and Civil Engineering, 21(7-8), 960-987 (2017).
31. Ngoma, J., Philippe, P., Bonelli, S., Radjai, F., Delenne, J.: Two-dimensional numerical simulation of chimney fluidization in a granular medium using a combination of discrete element and lattice Boltzmann methods. Phys. Rev. E. 052902, 1–23 (2018).
32. Benseghier, Z., Cuéllar, P., Luu, L. H., Delenne, J. Y., Bonelli, S., Philippe, P.: Relevance of free jet model for soil erosion by impinging jets. Journal of Hydraulic Engineering, 146(1), 04019047, (2020).
33. Benseghier, Z., Cuéllar, P., Luu, L.-H., Bonelli, S., Philippe, P.: A parallel GPU-based computational framework for the micromechanical analysis of geotechnical and erosion problems. Computers and Geotechnics, 120, 103404, (2020).
34. Leonardi, A., Pirulli, M.: Analysis of the load exerted by debris flows on filter barriers: Comparison between numerical results and field measurements. Comput. Geotech. 118, 103311 (2020).
35. Wang, H., Zhao, H., Guo, Z., He, Y., Zheng, C.: Lattice Boltzmann method for simulations of gas-particle flows over a backward-facing step. J. Comput. Phys. 239, 57–71 (2013).
36. Leonardi, A., Goodwin, G.R., Pirulli, M.: The force exerted by granular flows on slit dams. Acta Geotech. 14, 1949–1963 (2019).
37. Anand, A., Curtis, J.S., Wassgren, C.R., Hancock, B.C., Ketterhagen, W.R.: Predicting discharge dynamics of wet cohesive particles from a rectangular hopper using the discrete element method (DEM). Chem. Eng. Sci. 64, 5268–5275 (2009).
38. Jiang, M., Zhang, W., Sun, Y., Utili, S.: An investigation on loose cemented granular materials via DEM analyses. Granular Matter. 15, 65–84 (2013).
39. Mcnamara, G.R., Zanetti, G.: Use of the boltzmann equation to simulate lattice-gas automata. Phys. Rev. Lett. 61, 2332–2335 (1988).
40. Bhatnagar, P.L., Gross, E.P., Krook, M.: A model for collision processes in gases. I. Small amplitude processes in charged and neutral one-component systems. Phys. Rev. 94, 511–525 (1954).
41. Chapman, S., Cowling, T. G., Burnett, D.: The mathematical theory of non-uniform gases: an account of the kinetic theory of viscosity, thermal conduction and diffusion in gases. Cambridge university press (1990).
42. Yan, Z., Yang, X., Li, S., Hilpert, M.: Two-relaxation-time lattice Boltzmann method and its application to advective-diffusive-reactive transport. Adv. Water Resour. 109, 333–342 (2017).
43. Ginzburg, I., d'Humières, D., Kuzmin, A.: Optimal stability of advection-diffusion lattice boltzmann models with two relaxation times for positive/negative equilibrium. J. Stat. Phys. 139, 1090–1143 (2010).
44. Cundall, P.A., Strack, O.D.: A discrete numerical model for granular assemblies. Geomechanics. 29, 47–65 (1979).

45. Cui, X., Li, J., Chan, A., Chapman, D.: A 2D DEM-LBM study on soil behaviour due to locally injected fluid. Particuology. 10, 242–252 (2012).
46. Jing, L., Yang, G.C., Kwok, C.Y., Sobral, Y.D.: Flow regimes and dynamic similarity of immersed granular collapse: A CFD-DEM investigation. Powder Technol. 345, 532–543 (2019).
47. Courrech du Pont, S., Gondret, P., Perrin, B., Rabaud, M.: Granular Avalanches in Fluids. Phys. Rev. Lett. 90, 044301 (2003).
48. Brunier-Coulin, F. Mécanismes élémentaires de l'érosion d'un sol cohésif. In Congrès français de mécanique. AFM, Association Française de Mécanique.(2015).
49. Noble, D.R., Torczynski, J.R.: A lattice-Boltzmann method for partially saturated computational cells. Int. J. Mod. Phys. C. 09, 1189–1201 (1998).
50. He, X., Zou, Q., Luo, L., Dembo, M.: Analytic solutions of simple flows and analysis of nonslip boundary conditions for the lattice Boltzmann BGK model. J. Stat. Phys. 87, 115–136 (1997).
51. Ting, B.J.M., Corkum, B.T.: Computational laboratory for discrete element geomechanics. J. Comput. Civ. Eng. 6, 129–146 (1992).